



HAL
open science

Evolution of the particle size distribution of tricalcium silicate during hydration by synchrotron X-ray nano-tomography

J Neubauer, T Sowoidnich, L Valentini, C Schulbert, C Naber, C Rößler, Julio Da Silva, F Bellmann

► To cite this version:

J Neubauer, T Sowoidnich, L Valentini, C Schulbert, C Naber, et al.. Evolution of the particle size distribution of tricalcium silicate during hydration by synchrotron X-ray nano-tomography. *Cement and Concrete Research*, 2022, 156, pp.106769. 10.1016/j.cemconres.2022.106769 . hal-03751622

HAL Id: hal-03751622

<https://hal.science/hal-03751622v1>

Submitted on 17 Aug 2022

HAL is a multi-disciplinary open access archive for the deposit and dissemination of scientific research documents, whether they are published or not. The documents may come from teaching and research institutions in France or abroad, or from public or private research centers.

L'archive ouverte pluridisciplinaire **HAL**, est destinée au dépôt et à la diffusion de documents scientifiques de niveau recherche, publiés ou non, émanant des établissements d'enseignement et de recherche français ou étrangers, des laboratoires publics ou privés.

1 **Evolution of the particle size distribution of tricalcium silicate during hydration by**
2 **synchrotron X-ray nano-tomography**

3 J. Neubauer^{a*}, T. Sowoidnich^b, L. Valentini^c, C. Schulbert^d, C. Naber^a, C. Rößler^b, J. DaSilva^e,
4 F. Bellmann^b

5

6 ^a Friedrich-Alexander Universitaet Erlangen-Nuernberg, GeoZentrum, Mineralogy,
7 Schlossgarten 5a, 91054 Erlangen, Germany

8 ^b Bauhaus-Universitaet Weimar, Finger-Institute for Building Materials, Coudraystr. 11A,
9 99423 Weimar, Germany

10 ^c University of Padua, Department of Geosciences, Via G. Gradenigo 6, 35131 Padua, Italy

11 ^d GeoZentrum Nordbayern, Section Palaeontology, Friedrich-Alexander Universitaet (FAU)
12 Erlangen-Nuernberg, Loewenichstraße 28, 91054 Erlangen, Germany

13 ^e European Synchrotron Radiation Facility, 71 avenue des Martyrs, CS 40220, 38043 Grenoble
14 Cedex 9, France

15 * corresponding author: juergen.neubauer@fau.de

16

17 **Abstract**

18 The particle size distribution of tricalcium silicate (C₃S) is essential for the modelling of early
19 C₃S hydration kinetics. In this study, this parameter is analysed during the main hydration
20 period until the first 20 h by synchrotron near-field ptychographic (NF-PXCT) and holographic
21 (HXCT) computed nano-tomography. Additionally, X-ray diffraction, ²⁹Si NMR, thermal
22 analysis, scanning electron microscopy, and inductively coupled plasma-optical emission
23 spectroscopy were used to investigate the system evolution. The time-dependent pore solution
24 composition is also provided to gain further information.

25 HXCT and NF-PXCT show comparable values regarding the evolution of the C₃S particle size
26 distribution during hydration, indicating that C₃S particles smaller than 1.3 µm are completely
27 dissolved after 20 h of hydration. The results can be reasonably reproduced by numerical
28 models if for all particle sizes a constant reacted rim thickness for each degree of hydration is
29 assumed. Data on the aqueous phase composition are also provided.

30 **Keywords**

31 Tricalcium silicate (D); hydration (A); synchrotron nano-tomography (B); near-field
32 ptychography (B); holography (B).

33

34

35 **1. Introduction**

36 The hydration of tricalcium silicate (Ca_3SiO_5 , C_3S in cement notation) has been investigated in
37 a large number of studies to understand the complex reactions that occur during the hydration
38 of ordinary Portland cement [1]. The products of reaction between C_3S and water (hydration)
39 are C-S-H and portlandite ($\text{Ca}(\text{OH})_2$, CH) [1].

40 The mechanism of C_3S hydration is consistently described as a dissolution-precipitation
41 process with precipitation of C-S-H on the surface of C_3S [2, 3]. Portlandite, in contrast, is
42 formed in the pore space between C_3S particles [4]. Hydration proceeds in stages with different
43 reaction rates called (pre)induction, main hydration period (consisting of acceleration and
44 deceleration) as well as the steady-state period [5]. Beyond this definition, there is no general
45 consensus on the mechanisms governing the kinetics. The present work attempts to provide
46 experimental data for these discussions, particularly on the causes of the deceleration period.
47 A general discussion of C_3S hydration kinetics is not within the scope of this paper but can be
48 found in [2]. To explain the onset of the deceleration period, a limited diffusion of ions from
49 the C_3S surface into the aqueous phase due to covering of the interface by growth of C-S-H
50 [5, 6] has been proposed. In addition, a reduction of the C_3S dissolution rate by consumption
51 of small C_3S grains [1, 7-9] that reduces the overall C_3S reaction rate is discussed as a rate-
52 determining factor during the deceleration period. The main difficulty is the direct
53 experimental observation of C_3S particles during hydration that are overgrown by C-S-H in
54 the presence of portlandite.

55 Gas adsorption measurements are state-of-the-art for the experimental determination of the
56 specific surface area of anhydrous cementitious materials. Alternatively, the surface area of
57 C_3S can be calculated from the particle size distribution, usually under the assumption that the
58 particles are spheres without consideration of the particle roughness. Laser scattering is
59 commonly applied to determine the particle size distribution of anhydrous cement/ C_3S .
60 Because gas adsorption and laser scattering are not phase selective, neither method can be
61 used to measure the C_3S specific surface area of hydrated samples because these contain
62 anhydrous and hydrous phases (C_3S , C-S-H and portlandite).

63 Imaging techniques such as electron and X-ray microscopy have high potential in the
64 experimental determination of the particle size distribution and thus the specific surface area
65 of C_3S during hydration. This is due to the ability of these methods to identify individual
66 particles in the microstructure. High resolution of scanning electron microscopy (SEM) can
67 be used to record 3D images of cementitious materials using focussed ion beam serial
68 sectioning [10]. The limiting factor is the small size of the analysed volume in the SEM, that is
69 often too small to deduce statistical relevant data for a variety of particle sizes [59, 60, 61]. For
70 X-ray microscopy, one can obtain the absorption and phase-contrast images of the sample for
71 larger volumes. The X-rays attenuated by the sample yield the absorption-contrast, whereas
72 the phase shifts between the incident and the transmitted wavefields, due to the X-rays
73 refraction by the sample, generate phase contrast images [11, 12]. The absorption-contrast
74 imaging of the individual phases, present in low-absorbing materials, consisting of atoms with
75 low atomic number is challenging. In this case, phase-contrast imaging can be used to achieve
76 a high compositional contrast within samples consisting of materials with similar linear
77 attenuation coefficients [13]. However, this property is only accessible by applying imaging
78 techniques using spatially coherent probe beams, such as 3rd-generation-synchrotron radiation

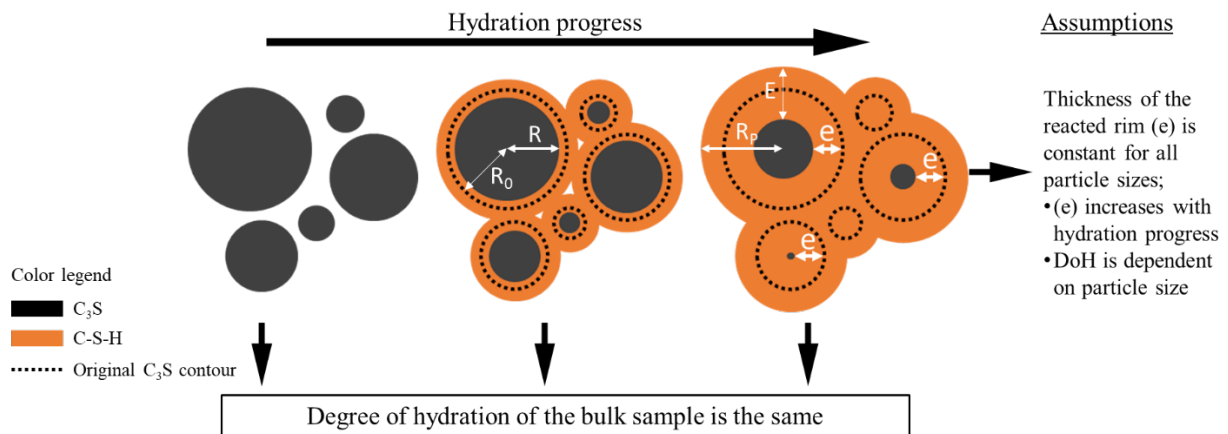
79 and electron beam or laser, which allows the generation of interference, and by the use of
80 appropriate phase retrieval algorithms.

81 For high resolution X-ray imaging (2D and 3D), the high brilliance of synchrotron radiation
82 was shown to be advantageous to study multi-hierarchical materials like cement pastes [14] in
83 scattering experiments [15-22] and spectroscopic investigations, both reviewed elsewhere
84 [12, 23-26]. In Holographic X-ray Computed Tomography (HXCT), the detector is placed at
85 4 different distances from the sample permitting the detection of both the incident and
86 refracted radiation (near-field inline holography). With this setup, the attenuation and the
87 phase shift can be detected. By varying the sample-detector distance, the phase of the wave
88 field can be determined (phase retrieval) solving a mathematically ill-posed problem. The 3D
89 information (tomography) is obtained by rotating the sample and recording images at a series
90 of projection angles for different sample-detector distances [13]. Synchrotron based HXCT was
91 used in several studies dealing with cement. These studies, for example, focussed on the
92 impact of organic admixtures (dispersants or (super)plasticizers) on the formation of C-S-H
93 during the hydration of ordinary Portland cement. The pore size distribution in the hardened
94 samples was also analysed [14, 27].

95 In Near-Field Ptychographic X-ray Computed Tomography (NF-PXCT), X-ray absorption and
96 X-ray phase-contrast imaging of the samples are obtained also in the holographic regime. The
97 near-field ptychographic approach is based on the acquisition of holograms of the sample at
98 different lateral positions within a structured incoming coherent beam to solve the ill-posed
99 problem in phase-retrieval [53]. With the use of appropriate phase retrieval algorithms,
100 NF-PXCT permits an inherent quantitative 3D imaging of the sample regarding the electron
101 density distribution and by that the mass density at voxel resolution below 20 nm [12, 28, 29].
102 Far-field Ptychographic X-ray Computed Tomography (FF-PXCT) was, for example, used to
103 determine the mass density of different phases in Portland cement pastes [30-32]. Another
104 study showed the distribution of C_3S , C-S-H, and portlandite in hardened C_3S pastes, proving
105 the strength of the method in phase contrast [11, 31]. The microstructure including AFm, AFt,
106 and aluminium hydroxide was analysed by PXCT in ye'elimite containing materials after
107 hydration [33]. PXCT experiments were also performed with the aim of determining the mass
108 density and to study the reaction of ye'elimite in-situ [34]. Finally, the radius of ettringite
109 needles formed during the hydration of C_3A in the presence of gypsum was investigated by
110 PXCT [35].

111 Although the experimental determination of the evolution of the particle size distribution of
112 C_3S remains a challenging task, hypotheses were proposed to address this important issue. In
113 the first hypothesis, it is assumed that the degree of hydration of the bulk material is equal to
114 that of the median particle size. Based on this assumption, the median particle radius was used
115 to calculate the reacted rim of C_3S (e), the C-S-H layer thickness (E) and the full particle size
116 (R_p , consisting of a C_3S core overgrown by C-S-H) [36] (abbreviations in Figure 1). The second
117 hypothesis deals with the formation of C-S-H fibres at the surface of C_3S during the
118 acceleration and deceleration period without assuming a diffusion barrier or impingement
119 ('needle model' [2]). Such models may account for a constant C-S-H layer thickness for all
120 particles at a given degree of hydration. The third hypothesis (Figure 1) states that the
121 hydration proceeds faster for small C_3S particles as a result of an identical reacted rim thickness
122 for all particle sizes. This reacted rim thickness increases with hydration progress ('reaction

123 zone hypothesis') [8]. The assumption of a constant reacted rim thickness was originally
 124 developed for the formation of a C-S-H layer around C_3S particles and is used here to describe
 125 the thickness of the dissolved layer from the C_3S particles. As a result, smaller particles are
 126 fully dissolved earlier than larger particles, and the degree of hydration of the bulk sample is
 127 unequally distributed over the different particle size classes. It should be clarified that the first
 128 hypothesis mentioned above deals only with the median particle size and not with the full
 129 particle size distribution. Furthermore, the calculation of the C_3S particle size distribution
 130 during the main hydration period is in principle possible with the 'needle model'. However,
 131 the input parameters need to be changed dramatically and are outside the range of reasonable
 132 values when this model is used for the present data. For these reasons, only the 'reaction zone
 133 hypothesis' is addressed in this work.



134

135 Figure 1: 'Reaction zone hypothesis' for the development of the particle sizes of C_3S during hydration with
 136 individual degree of hydration of each particle size due to constant reacted rim thickness. R_0 -radius of the
 137 anhydrous particle, R -radius of the hydrated particle, e -reacted rim, E -C-S-H layer thickness, R_p -radius of the full
 138 particle (C_3S core + C-S-H layer). The presentation focuses on details important to the present study; additional
 139 information such as formation of a gap between remaining C_3S cores and C-S-H or the difference between inner
 140 and outer C-S-H are not included to increase clarity of the presentation.

141 The first aim of the present work is to fill the mentioned experimental gaps regarding the
 142 measurement of the specific surface area of C_3S during the main hydration period. Therefore,
 143 the C_3S particle size distribution is measured by state-of-the-art 3D X-ray nanoimaging
 144 technology, uniquely available in 3rd generation synchrotron facilities such as ESRF including
 145 the novel near-field ptychographic X-ray computed tomography (NF-PXCT) and holographic
 146 X-ray computed tomography (HXCT). The present work is thus the first application of NF-
 147 PXCT for characterization of cementitious samples. The used techniques provide an
 148 unprecedented high sensitivity to sample morphology and unprecedented high resolution to
 149 study dynamics in cement. Thereby, the particle size distribution data are obtained from the
 150 analysis of local distribution of the particle morphology by measuring each particle
 151 individually.

152 The second aim of the present work is to evaluate the 'reaction zone hypothesis' by simulation
 153 of the development of the C_3S particle size distribution during hydration based on the
 154 gathered data. The degree of hydration of C_3S is needed as an input parameter for this purpose,
 155 which is independently analysed by X-ray diffraction (XRD), ^{29}Si nuclear magnetic resonance
 156 spectroscopy (NMR) and thermal analysis (TA). Additionally, the C-S-H layer thickness at the
 157 C_3S surface is evaluated by SEM imaging. The latter approach is complicated by the fact that

158 SEM is a 2D-method which is discussed in section 3.2. The reliability of the ‘reaction zone
159 hypothesis’ is explored by comparison of the measured and predicted control parameters: C₃S
160 particle size distribution and specific surface area of C₃S. The aqueous phase composition is
161 measured by means of inductively coupled plasma-optical emission spectroscopy (ICP-OES)
162 during the main hydration period. Combination of the various results allows us to discuss the
163 development of the C₃S particle size distribution during hydration with additional
164 information on the liquid phase composition.

165

166 **2. Materials and methods**

167

168 **2.1 Raw material preparation and properties**

169 **2.1.1 Synthesis of tricalcium silicate**

170 Tricalcium silicate was produced by high temperature solid state reaction from a blend of
171 calcium carbonate (Merck p.a.) and highly dispersed silicon dioxide (Merck p.a.). The raw
172 materials were homogenized and fired at 1520 °C for 8 hours in a platinum crucible and
173 subsequently quenched at 20 °C. This procedure was repeated twice and the material was
174 ground between the high temperature treatments to improve its homogeneity. For high
175 resolution synchrotron X-ray tomography, the volume of the sample has to be very small. To
176 guarantee that a sufficient number of particles are in that volume, the particle size of the C₃S
177 has to be below 10 μm. For this purpose, the material was ground in batches of 25 g for 20 min
178 in a zirconia disk mill at 700 rpm under the addition of 0.08 g diethylene glycol as a grinding
179 aid. The particle size was further reduced in an air classifier to remove particles larger than 10
180 μm. The individual batches of C₃S were finally homogenized. The particle size distribution
181 measured by Laser scattering is provided in the supplementary information (Figure S1). These
182 results cannot be directly compared to the particle size distribution obtained by X-ray
183 tomography as both methods are based on different physical methods and use different
184 definitions to extract the particle size from the experimental data.

185 The C₃S produced in this study has the following chemical composition (determined by
186 chemical wet analysis based on titration of calcium , gravimetric determination of silicon as
187 well as ICP-OES analysis for all other elements except silicon): 72.8 wt.-% CaO, 26.1 wt.-% SiO₂
188 and 1.0 wt.-% LOI, whereas the concentration of foreign oxides was below the limit of
189 detection (0.1 wt.-%). The free lime concentration determined by Franke-method [37] was 0.3
190 wt.-%. Analysis by QXRD indicated the presence of pure C₃S in the triclinic modification and
191 the concentration of belite and free lime were below the limit of quantification (LOQ: 5 wt.-%
192 for belite and 0.5 wt.-% for CaO).

193 **2.1.2 Hydration of C₃S**

194 All experiments were designed to match the requirements of synchrotron X-ray nano-
195 tomography. As stated before, particle sizes below 10 μm are specifically prepared in order to
196 increase the spatial resolution of the tomography. Therefore, a relatively high water/C₃S-ratio
197 (by mass) of 3.0 was required to produce a workable suspension as the surface area of the

198 starting material is very high. This water/solid-ratio is higher than normally used for
199 hydration studies on pastes but it was recently confirmed that hydration kinetics of C₃S are
200 not affected by the water/solid-ratio [58]. Accordingly, 15 g of C₃S was mixed with 45 g filtered
201 saturated calcium hydroxide solution and 0.10 g superplasticizer. Superplasticizer (SP1 from
202 reference [38]) was added to the starting solution prior to mixing to avoid the formation of
203 agglomerates due to the surface charge of the C₃S particles [39, 40]. This superplasticizer is a
204 methacrylic acid-co-polyethylene glycol type polycarboxylate with the following parameters:
205 8.2 repeating units, 3.9 monomers per repeating unit, 23 monomers in the side chain with a
206 total molecular weight of 10,930 g/mol.

207 The closed vessel filled with the suspension was stirred for 24 hours at a temperature of 25 °C.
208 Samples (approx. 6 ml suspension) taken after 4, 8, 12, and 16 hours of hydration were filtered
209 in a gaseous nitrogen pressure filtration unit using filters with a pore width of 15 nm. This
210 relatively small pore width of the filter was used to avoid C-S-H particles from passing
211 through the filter, especially when superplasticizers are present [38]. As a consequence, the
212 filtration process took 30-45 min at a pressure of approx. 2 bar. The solid residue of the
213 filtration was dried at 60 °C for X-ray nano-tomography, QXRD, ²⁹Si-NMR, SEM, and thermal
214 analysis. It was not possible to extract pore solution after 20 and 24 hours by this method.
215 Additional samples (< 100 mg) were taken after 6, 10, 14, 18, and 22 hours only for thermal
216 analysis by drying at 60 °C without prior filtration.

217 **2.1.3 Preparation of the hydrated C₃S samples for Scanning Electron Microscopy (SEM)**

218 Sample preparation for SEM characterisation included embedding of the hydrated samples in
219 epoxy resin and mechanical polishing using diamond slurries of 15, 9, 3, and 1 μm particle
220 size. The polished samples were coated with gold to ensure electric conductivity of the sample
221 surface.

222 **2.1.4 Preparation of the hydrated C₃S samples for synchrotron X-Ray nano-tomography**

223 The samples for synchrotron X-ray nano-tomography were produced by embedding the
224 samples in a commercial two-component epoxy resin. Thin filaments composed of epoxy resin
225 and sample material were pulled while the epoxy-C₃S mix was already stiff but still workable.
226 After hardening of these filaments containing the samples embedded in epoxy resin, these
227 were cut into small segments with a length of 1-2 mm. Segments with a diameter of
228 approximately 100 μm were selected under an optical microscope and glued to the sample
229 post of the device by epoxy resin. Thus, the final length of the filaments was approximately 1
230 mm and the diameter was approximately 100 μm. Only the anhydrous C₃S was mixed with a
231 highly adsorbing polymer before embedding in resin as described before. This was done to
232 produce an organic film on the surface that enables the observation of individual C₃S particles
233 instead of agglomerates. For this purpose, 1.00 g C₃S was mixed with 2.00 g polymer
234 dispersion (styrene-acrylate co-polymer model latex in [41]) and treated by ultrasound
235 (frequency: 20 kHz, amplitude 43 mm) for 20 seconds and quickly dried after 1 minute at 50 °C
236 to avoid a reaction with water. A schematic illustration of the sample preparation steps and
237 the nano-tomography as well as simulation is provided in the supplementary information
238 (Figure S2).

239

240 2.2 Analytical methods

241 2.2.1 Degree of hydration of C₃S and aqueous phase composition during hydration

242 X-ray diffraction

243 XRD patterns of the hydrated samples were obtained in a D8 Advance diffractometer
244 (BRUKER-AXS) equipped with a LynxEye detector using a Cu-tube operating at 40 mA and
245 40 kV. The scans from 7 to 70 °2θ were recorded with a step size of 0.011 °2θ and a counting
246 time of 0.5 seconds per step. The concentration of individual phases was calculated using the
247 Rietveld-software Topas 5.0 (BRUKER-AXS), using a recently developed external standard
248 method [42, 43]. The respective crystal structures were applied to describe the tricalcium
249 silicate [44] and portlandite [45] contribution to the diffraction pattern, while a PONKCS
250 approach by Bergold et al. [46] was employed to describe the C-S-H contribution. The
251 amorphous content in the anhydrous tricalcium silicate was not increased by the intense
252 milling.

253 Thermal analysis (TA)

254 Thermogravimetry data were obtained in a TA instruments SDT Q600 device at a heating rate
255 of 10 K/min under a stream of nitrogen. The water content of C-S-H was determined by
256 subtraction of the change in mass related to dehydration of portlandite and the decarbonation
257 of calcium carbonate from the loss on ignition at the final temperature (1000 °C). It was
258 revealed in this calculation that the C-S-H of the hydrated C₃S sample contains 2.6 moles of
259 water. Under the assumption of a Ca/Si molar ratio of 1.7 for C-S-H, the hydration reaction of
260 C₃S can be written as:



262 Equation 1 was used for the calculation of the C₃S content in the hydrated samples.

263 ²⁹Si-NMR spectroscopy

264 ²⁹Si solid-state magic angle spinning (MAS) nuclear magnetic resonance (NMR) spectroscopy
265 was performed in a spectrometer equipped with an Oxford wide bore magnet (11.7 T), a
266 Bruker Avance III 500 console and a Doty triple resonance probehead for 7 mm (O.D.) zirconia
267 rotors.

268 Single-pulse and cross-polarization (²⁹Si{¹H} CP) experiments were conducted by ²⁹Si solid-
269 state NMR to quantify the concentrations of C₃S, C-S-H and metastable hydrate phase [47],
270 which can be interpreted as a first form of C-S-H [48]. The single-pulse experiments used a
271 MAS spinning rate of 4 kHz, a π/2 pulse length of 6.4 μs, 128 scans, and a recycle delay time
272 of 600 s. This recycle delay time is too short for complete relaxation of the silicon sites in C₃S
273 resulting in an underestimation of the intensity of this phase compared to C-S-H which has a
274 much lower relaxation time. Thus, the intensities extracted from the deconvolution need to be
275 multiplied by a factor of 3.62, which was obtained by comparing a fully relaxed spectrum
276 (recycle delay time 4 hours, 24 scans) with a spectrum acquired at the same degree of relaxation
277 (recycle delay time 600 s, 24 scans) as the samples used for quantitative analysis. The chemical
278 shifts associated to the different phases and the recorded spectra obtained by the single-pulse
279 experiments are provided in the supplementary information (Figure S3).

280 The $^{29}\text{Si}\{^1\text{H}\}$ CP experiments were conducted using parameters that were adjusted using a
281 sample of $\alpha\text{-C}_2\text{SH}$ at the same MAS frequency of 4 kHz. The spectra were recorded using an
282 initial ^1H pulse ($\pi/2$ pulse length of 4.5 μs), a contact time of 4 ms with a ^1H rf field strength
283 of 38.3 kHz (ramp 10090) and a ^{29}Si rf field strength of 30.9 kHz, ^1H decoupling during
284 acquisition for 10 ms, a recycle delay time of 3 s and 1024 scans.

285 The concentration of C_3S , C-S-H, and a metastable hydration product containing Q^0 sites was
286 computed from the (corrected) relative intensities from the deconvolution of the spectra, the
287 silicon concentration in the sample and the molar weight of the phases. The molar weight of
288 C-S-H and the metastable hydration product is based on the composition of these phases
289 assuming $1.7 \text{ CaO} \cdot \text{SiO}_2 \cdot 2.6 \text{ H}_2\text{O}$ and $1.3 \text{ CaO} \cdot \text{SiO}_2 \cdot 2\text{H}_2\text{O}$ [48], respectively.

290 All chemical shift data are reported relative to tetramethylsilane (TMS) as an external
291 standard. The software DMFit was used for the deconvolution of the spectra [49].

292 The $^{29}\text{Si}\{^1\text{H}\}$ MAS NMR (CP) spectra and the chemical shifts of the phases are presented in the
293 supplementary information of this article (Figure S4 & S5, Table S2).

294 ICP-OES

295 Ion concentrations in the filtered aqueous solutions were analysed by ICP-OES using a Horiba
296 Jobin Yvon, active M with radial observation. Calcium and silicon concentrations were
297 measured at a wavelength of 373.69 nm and 251.61 nm, respectively. The aqueous phase was
298 obtained by filtration of the suspensions after 4 h, 8 h, 12 h, and 16 h of hydration. The filtered
299 solutions were diluted and stabilized by the addition of 0.2 g of 5 M HNO_3 for analysis by
300 means of ICP-OES. This dilution was taken into account.

301 2.2.2 C-S-H layer analysis by means of Scanning Electron Microscopy (SEM)

302 Microstructural characterisation was carried out using a SEM equipped with a field emission
303 gun (Nova NanoSEM 230 FEI). For the detection of backscatter electron images, 12 kV
304 acceleration voltage and 1.8 nA probe current were used (high vacuum mode of the
305 instrument). The C-S-H layer thickness was measured by manually selecting undisturbed (by
306 sample preparation and vacuum) hydration rims. For each sample more than 50 particles have
307 been analysed. It is known that C-S-H can lose water when exposed to high vacuum but it is
308 not expected that the morphology is significantly affected by this dehydration (measurements
309 were taken in areas where no significant shrinkage cracking was observed).

310 2.2.3 C_3S particle size distribution during hydration by holo- and near-field ptychographic 311 nano-tomography using synchrotron radiation

312 The experiments were carried out at the ID16A nano-imaging beamline of the European
313 Synchrotron Radiation Facility (ESRF) [50]. This end-station is optimized for efficient hard
314 X-ray nano-focusing and designed to provide coherent X-rays for nanoimaging. During the
315 experiments, the sample was exposed to vacuum (around 10^{-7} mbar) at room temperature.
316 However, the C_3S and C-S-H particles are not directly exposed to the vacuum and subsequent
317 water loss as the material is fully enclosed in epoxy resin. The beamline offers a piezo-driven
318 short-range hexapod stage for the accurate positioning and scanning of the sample under the
319 control of capacitive sensors. Two sets of tomographic experiments were conducted, namely,

320 HXCT and NF-PXCT. Details of the experiments using those two techniques are given in the
321 supplementary information of this article.

322

323

324 3. Results

325

326

327 3.1 Degree of hydration of C₃S and aqueous phase composition during hydration

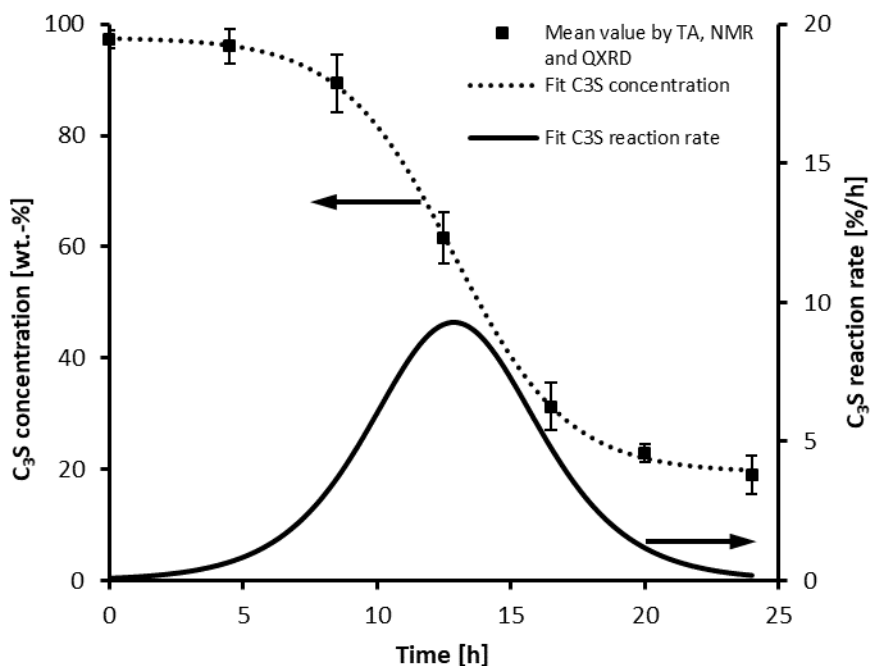
328 The samples obtained during the hydration experiment were analysed by three independent
329 methods to determine the degree of hydration. These include QXRD, ²⁹Si MAS NMR
330 spectroscopy, and thermal analysis. The degree of hydration is calculated from the evolution
331 of the concentration of tricalcium silicate in the samples when using QXRD and ²⁹Si NMR. In
332 contrast, the C₃S concentration is indirectly assessed by thermal analysis by using the
333 determined concentrations of C-S-H and portlandite to stoichiometrically calculate the C₃S
334 concentration (equation 1). The concentration of C₃S during hydration is plotted in Figure 2 as
335 the mean value, with the corresponding standard deviation obtained from the individual
336 methods. A method-dependent list of these results is provided in the supplementary
337 information of this article (Table S1). The mean value of the C₃S concentration against time is
338 fitted using Equation 2:

$$339 \quad C_3S \text{ [wt. -\%]} = A2 + \frac{(A1-A2)}{1+e^{-\frac{t-t_0}{dt}}} \quad \text{Equation 2}$$

340 A corrected R² = 0.99955 was achieved with the fit parameters A1 = 97.6 wt.-%, A2 = 19.5 wt.-%,
341 t₀ = 12.9 h and dt = 2.1 h. This mathematical fit is also given in Figure 2 (dotted line). The first
342 derivative of this fit corresponds to the reaction rate and is plotted on the right axis of Figure
343 2. The application of reaction calorimetry that is generally used for the determination of the
344 hydration rate [1] was not possible because the hydration was performed in suspensions
345 (water/C₃S - ratio (by mass) of 3.0) and thus continuous stirring is needed during the
346 measurement.

347 As shown in Figure 2, the concentration of C₃S at the start of the experiment is slightly lower
348 than 100 wt.-%. This can be the consequence of the adsorption of a small amount of water in
349 the air classifier during milling or other procedures. Between 5 and 20 h, the concentration of
350 C₃S drops to a final value of 19 wt.-% as it is consumed during the main hydration period.
351 Such a high degree of reaction (0.81) is attributed to the very small particle sizes of the used
352 C₃S powder. The maximum rate of reaction during the main hydration period is observed after
353 approximately 13 hours. This is relatively late when compared to other studies using pure
354 tricalcium silicate and the shift of the maximum of the main hydration peak is connected to
355 the addition of superplasticizer that is known to retard the nucleation and growth of C-S-H.
356 However, the retarding effect is relatively low as the concentration of superplasticizer was
357 only 0.67% relative to C₃S. Between 20 and 24 hours, the concentration of C₃S decreases from

358 23 to 19 wt.-%, indicating that the reaction has slowed down and the main hydration period
359 has ended.



360

361 Figure 2: C₃S concentration during 24 h of hydration given as the mean value from TA, NMR, and QXRD
362 measurements (black squares) with its mathematical fit by Equation 2 (dotted line), and C₃S reaction rate as the first
363 derivative (multiplied by -1) of the C₃S concentration fit (bold line, right hand axis).

364 In addition to the C₃S concentration, the aqueous phase of the C₃S suspensions during
365 hydration was analysed by ICP-OES (Table 1). The results show that the calcium ion
366 concentration is already at a very high level after 4 hours hydration (32 mmol/L) and increases
367 after 8 h to 34 mmol/L. At later hydration times, the calcium ion concentration in the aqueous
368 phase decreases, which can be attributed to nucleation and growth of portlandite [51]. A
369 calcium ion concentration of 28 mmol/L was observed after 16 hours reaction. The silicon
370 concentration displays an opposite trend compared to the calcium ion concentration,
371 decreasing from 20 to 16 μmol/L between 4 and 8 hours. A slight increase in silicon is observed
372 after 12 hours, followed again by a decrease after 16 hours. A possible explanation of the
373 observed trends in the ion concentrations of the aqueous phase can be deduced from the plot
374 of Si against Ca (Figure S7, supplementary information). In this way the results can be
375 interpreted that the aqueous phase is close to an equilibrium with a metastable C-S-H [48] for
376 hydration periods up to 12 h and departs towards stable C-S-H [52] at later hydration times.

377 3.2 C-S-H layer analysis by means of SEM

378 The hydrated samples were investigated by SEM with the aim of evaluating the C₃S particle
379 size distribution and the C-S-H layer thickness at the surface of the C₃S particles during
380 hydration. Figure 3 shows examples of these SEM investigations.

381 The dark areas in the SEM images shown in Figure 3 represent the epoxy resin, which was
382 used to fix the material. The C₃S particles are light grey, C-S-H is slightly darker covering the
383 C₃S surface. Portlandite can be recognised by its shape, i.e., as elongated shapes resulting from
384 sectioned plate-like crystals. Mean values of the C-S-H layer thickness were estimated for a

385 number of 57 (12 h), 77 (16 h), and 70 (20 h) C_3S particles providing the sum of inner and outer
386 C-S-H. These analyses provide only semi-quantitative information as the polishing process
387 during sample preparation cuts the particles not through the volume centre. An extraction of
388 the true thickness of the C-S-H layer from these results is not straightforward and requires a
389 number of assumptions for particle shape and other properties [54]. It is also complicated by
390 the fact that the C_3S particles have irregular shapes and there is a high variation in the thickness
391 of the C-S-H layer even at the same grain. Thus, an evaluation of accurate quantitative
392 information is complicated but a semi-quantitative approach demonstrates a growing
393 thickness of the C-S-H layer around tricalcium silicate during hydration as predicted by the
394 reaction zone hypothesis in Figure 1. Image analysis of the sample hydrated for 12 h shows
395 that the C-S-H covering the C_3S particles has the lowest thickness of the investigated samples
396 with a value of 300 ± 80 nm. This C-S-H layer thickness increases after 16 h of hydration to a
397 mean value of 670 ± 170 nm and after 20 h of hydration to 800 ± 260 nm. Although these results
398 bear a large error, the conducted SEM investigations prove the findings [4, 53] that the C-S-H
399 layer thickness increases with increasing hydration time. The values obtained for the C-S-H
400 layer thickness are much higher than the C-S-H needle length results summarized in [2] but in
401 broad agreement with layer thicknesses expected from BNG simulations [8]. The deviation
402 from values reported in [2] may be due to the fact that the C_3S used in this study had a higher
403 surface area, which resulted in a higher degree of hydration which facilitates formation of
404 longer C-S-H needles. It was also attempted to extract the particle size distribution of
405 tricalcium silicate from the SEM micrographs. These efforts have indicated that the size of the
406 C_3S cross sections can be analysed accurately by SEM but a recalculation of the diameter of the
407 3D-particles from the 2D cross sections is challenging due to irregular shaped alite cores. In
408 addition to C_3S and C-S-H, also portlandite particles are observed in all samples, especially in
409 the 20 h sample.

410

411

412

413

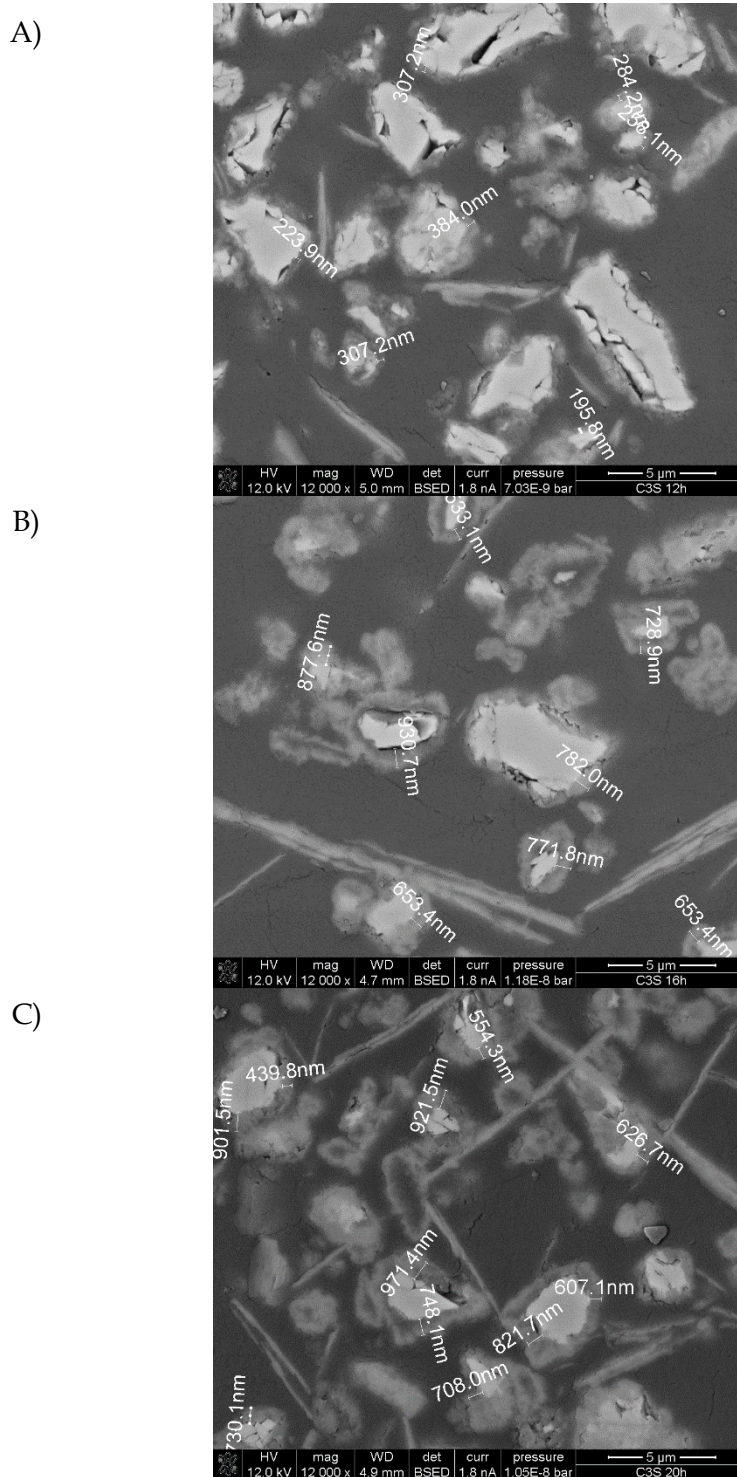
414

415

416

417

418

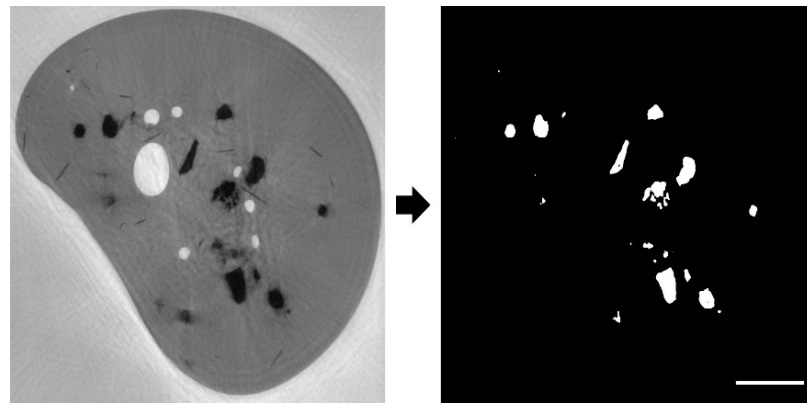


419 Figure 3: SEM images of embedded samples hydrated for 12 h (A), 16 h (B), and 20 h (C) with measurements of the
 420 C-S-H layer thickness.

421 **3.3 C₃S particle size distribution during hydration by holo- and near-field ptychographic**
 422 **tomography using synchrotron radiation**

423 The first step in determining the particle size distribution of C₃S during hydration is the
 424 identification of the C₃S particles in the samples. Figure 4 provides a greyscale image from the
 425 HXCT (left hand) together with the processed binary image obtained by the used segmentation
 426 algorithm (right hand) [55]. It can be seen that the used segmentation algorithm showed a
 427 good performance in separating neighbouring particles and removing hydration products.

428

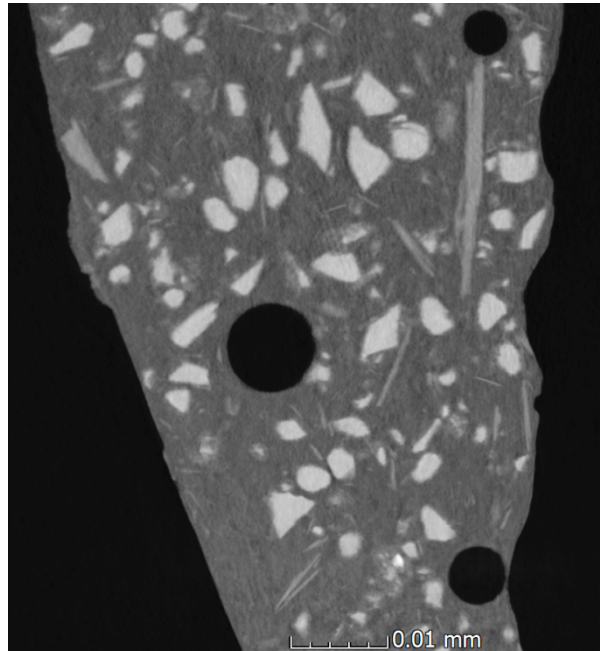


429

430 Figure 4: Grayscale (left) and binary (right) images relative to a 2D section through the reconstructed volume
431 (12-hours hydrated sample). Black: cement particles; grey: glue; white: air voids. Segmented C₃S particles in the
432 binary image are shown in white. Scale bar: 10 μm.

433 The image processing from the NF-PXCT experiments is exemplarily shown in Figure 5 for
434 the sample hydrated for 12 h. The C₃S particles appear in light grey, whereas C-S-H and
435 portlandite are dark grey and the resin still darker. Air bubbles are black spheres. The
436 hydration products C-S-H and portlandite have almost the same grey-level but a different
437 morphology as calcium hydroxide forms elongated particles of several micrometers in the
438 longest dimension. Figure 5 shows that the C₃S particles are clearly identified as their grey
439 level is different from all other phases in the analysed volume. These differences in grey level
440 between C₃S and the other phases allow an extraction of the particle size distribution of
441 tricalcium silicate. A related analysis of the C-S-H shell thickness is complicated by the fact
442 that the grey levels of C-S-H and portlandite are almost identical. The processed images were
443 segmented to identify the phase present in the individual voxel from the grey level. A
444 minimum of 8 connected voxels representing tricalcium silicate was considered as the smallest
445 particle size which could be identified in the segmentation process. These 8-voxel clusters at
446 an individual voxel size of 50 nm reveal the volume of the smallest particles which is 10⁶ nm³.
447 The diameter of a sphere with the identical volume is 124 nm. All particle diameters
448 determined from nano-tomography data which are presented in the following sections are
449 calculated as spheres with identical volume compared to the analysed volume of the irregular
450 shaped particles.

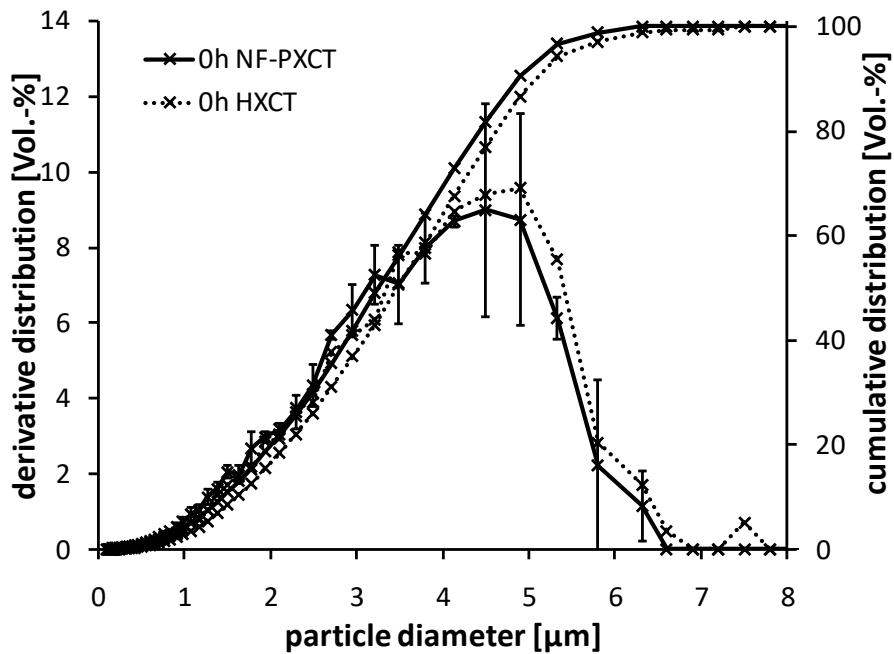
451



452

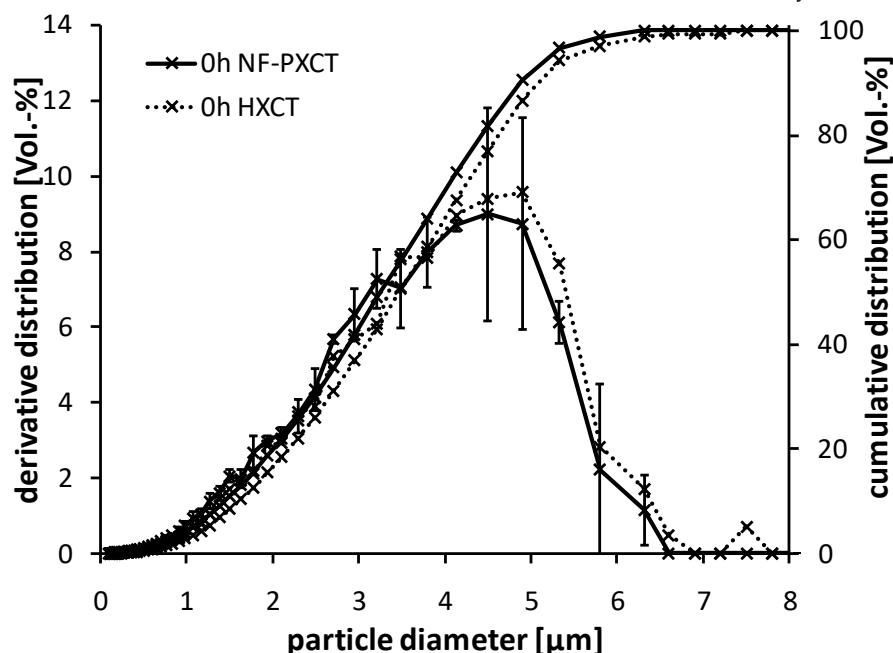
453 Figure 5: 2D view of the C₃S sample hydrated for 12 h showing irregular shaped C₃S particles, elongated portlandite
 454 sections, C-S-H as a hydration rim around tricalcium silicate, epoxy resin and air (black).

455 In the following, the identified C₃S particles were converted into particle size distributions.
 456 The volume distributions of the anhydrous C₃S particles are shown in Figure 6 obtained by
 457 HXCT and NF-PXCT.



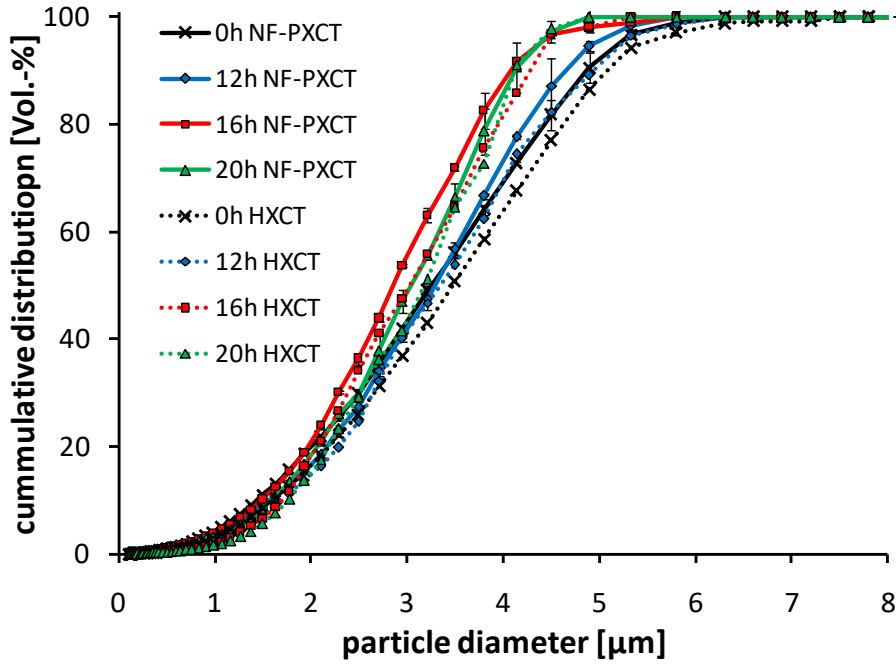
458

459 Figure 6: Volume-based particle size distribution (cumulative and derivative) for HXCT and NF-PXCT
 460 measurements of anhydrous C₃S.



461
 462 Figure 6 shows that NF-PXCT and HXCT give comparable results for the volume-based
 463 particle size distribution of the anhydrous C₃S. The maximum C₃S particle diameter is 6.3 μm
 464 (NF-PXCT) and the smallest measures 124 nm as defined during the post-processing
 465 procedure (minimum 8 voxels per particle are selected to avoid any possible contamination of
 466 the dataset due to the presence of noise). The HXCT results show some variation in grey level
 467 intensity complicating the segmentation process. It appears from the HXCT data that a 7.5 μm
 468 particle is present in the analysed volume which is not identified by NF-PXCT. A closer
 469 comparison of the tomographic data reveals that such a particle is not present but consists of
 470 an agglomeration of two particles in the HXCT reconstruction. This confirms the improved
 471 resolution and an enhancement in grey-level contrast of the NF-PXCT results compared to
 472 HXCT.

473 Results in Figure 7 show that the maximum particle size is reduced from 6.3 μm in the
 474 anhydrous sample to 5.5 μm (NF-PXCT) or 5.9 μm (HXCT) after 12 h of hydration. The same
 475 agreement between NF-PXCT and HXCT is observed for the other samples. The data also
 476 reveal a further decrease of the maximum particle size to 5.4 μm (NF-PXCT) or 5.1 μm (HXCT)
 477 after 16 h of hydration and the maximum particle size is 4.8 μm (NF-PXCT and HXCT) after
 478 20 h of hydration. This implies that the impact of hydration is clearly visible by a reduced
 479 diameter of the largest particles. The situation is different for small particles sizes as the
 480 number of particles in a given size class is reduced by dissolution of initially anhydrous
 481 particles and increased by size reduction of particles of initially larger particles during
 482 hydration. Overall, for the observed hydration periods, both effects lead to steeper and
 483 narrower particle size distribution as shown in Figure 7. The qualitative trend to smaller
 484 particles sizes during hydration observed for the largest particles is not evident in all size
 485 classes for all hydration times. Unexpectedly, the relative concentration of medium sized
 486 particles is higher in the 20 hours sample than in the 16 hours sample.



487

488 Figure 7: Volume-based cumulative particle size distribution obtained from NF-PXCT and HXCT measurements of
 489 C_3S .

490

491

492 **4. Discussion**

493

494 A hydration time dependent particle size distribution measurement during C_3S hydration
 495 with full phase selectivity was achieved in this study by employing synchrotron X-ray nano-
 496 tomography. As mentioned in the introduction, this experimental data was unavailable up to
 497 now for a description of the C_3S hydration. The obtained data on the development of the
 498 particle size distribution are used to evaluate the ‘reaction zone hypothesis’. This hypothesis
 499 claims that the hydration proceeds in an identical reacted depth (rim) for all sizes of particles
 500 (Figure 1). This reacted rim increases with the degree of hydration. The mathematical
 501 expressions are developed in the following equations.

502 **4.1 Mathematical expression**

503 With the reacted rim thickness e (Figure 1) and the initial diameter of particles of class i
 504 (denoted $D_i(0)$), the diameter of the particle of class i at distinct degree of hydration $D_i(\alpha)$ is:

505
$$D_i(\alpha) = D_i(0) - 2e \quad \text{Equation 3}$$

506 With:

507
$$2e \leq D_i(0) \quad \text{Equation 4}$$

508 From $D_i(\alpha)$, the mass of particle of class i (m_i) can be calculated using the corresponding volume
 509 of a sphere and the mass density of C_3S (3.16 g/cm^3). The degree of hydration of particle of
 510 class i at time t , $\alpha_i(t)$, reads:

$$511 \quad \alpha_i(t) = 1 - \frac{m_i(t)}{m_{i,0}} \quad \text{Equation 5}$$

512 With $m_i(t)$ and $m_{i,0}$ being the mass of the particle i at time t and at time zero, respectively.

513 The sum over all particles classes i weighted by the number of particles in each class N_i of the
 514 initial bulk sample gives the degree of hydration of the bulk sample $\alpha(t)$:

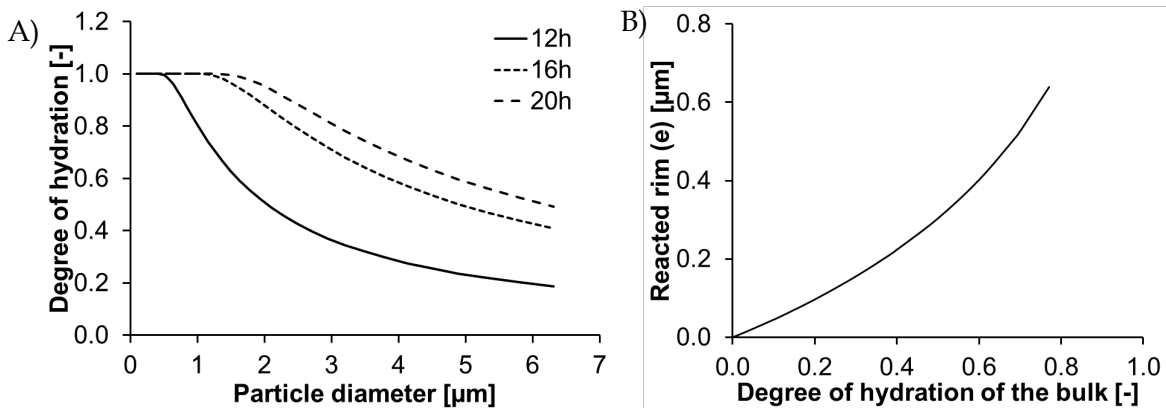
$$515 \quad \alpha(t) = 1 - \frac{\sum_{i=1}^n m_i(t)N_i}{\sum_{i=1}^n m_{i,0}N_i} \quad \text{Equation 6}$$

516 During simulation, the reacted rim thickness e is iterated until the global degree of hydration
 517 of the particles matches the measured degree of hydration at time t of the bulk sample ($\alpha(t)$,
 518 eq. 6, depicted in Figure 2). The result of this simulation gives the reacted rim thickness e and
 519 the degree of hydration distributed over all particle sizes.

520 4.2 Application

521 For the following simulation, the measured particle size distribution (NF-PXCT only) of the
 522 reference sample and the degree of hydration of the bulk samples are used as input
 523 parameters. Figure 8A shows the degree of hydration of the bulk samples distributed over all
 524 C_3S particle sizes calculated from eq. 5 for the samples hydrated for 12 h, 16 h, and 20 h. In
 525 Figure 8B, the corresponding reacted rim thickness 'e' is presented.

526 The simulation in Figure 8A shows that the C_3S particles with diameter smaller than $0.42 \mu\text{m}$
 527 have completely reacted after 12 h of hydration. The degree of hydration of particles with
 528 diameter ranging from $0.40 \mu\text{m}$ to $6.31 \mu\text{m}$ decreases from 1.0 to 0.2 non-linearly. After 16 h of
 529 hydration, particles smaller than $0.98 \mu\text{m}$ have completely reacted and after 20 h this value is
 530 $1.22 \mu\text{m}$. The simulated values for the distribution of the degree of hydration over the initial
 531 particle sizes (Figure 8A) correspond at the same time to the reacted rim thickness, which is
 532 depicted in Figure 8B. It can be seen that the reacted rim increases non-linearly with increasing
 533 degree of hydration.



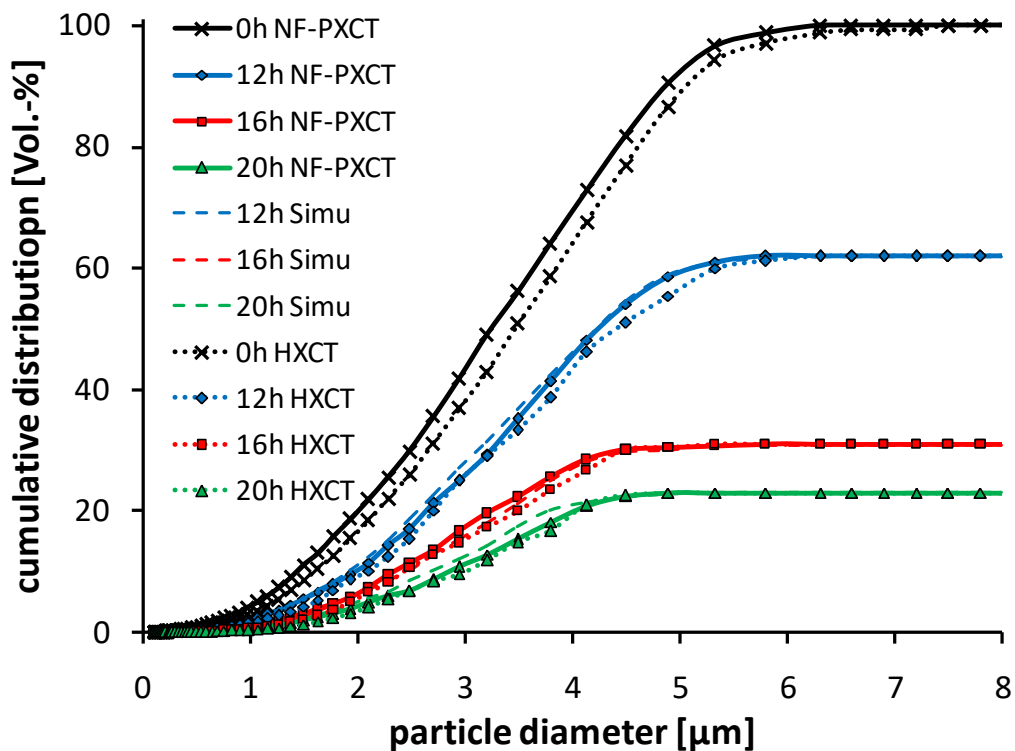
534 Figure 8: Simulated degree of hydration of the C_3S particles in dependence of their size after 12 h, 16 h, and 20 h of
 535 hydration (A). Calculated reacted rim thickness of the C_3S particles in dependence on the degree of hydration (B).

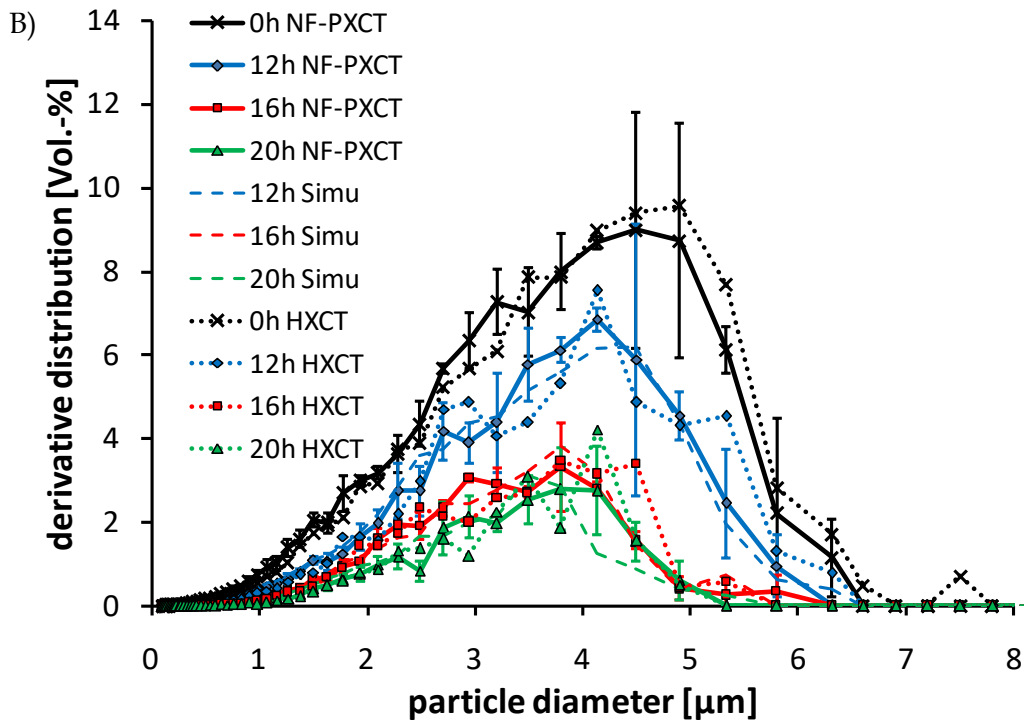
536 **4.3 Evaluation**

537 The 'reaction zone hypothesis' is qualitatively evaluated by comparing the measured values
538 of the C-S-H layer thickness and the particle size distribution in the following. A quantitative
539 evaluation will be presented afterwards by the comparison of the measured and predicted
540 specific surface area of C₃S during hydration.

541 **4.3.1 Qualitative evaluation of the simulation**

542 The qualitative evaluation step regarding the simulation based on the 'reaction zone
543 hypothesis' centres around the comparison of the predicted and measured particle size
544 distribution of C₃S during hydration. In addition to the particle size distribution of the starting
545 material (measured by NF-PXCT), also the degree of hydration of the samples is taken into
546 account as an input parameter. From this, the volume fractions of C₃S in the size classes i can
547 be calculated for the hydrated samples. The results of this calculation are compared to the
548 measured values in Figure 9.





549 Figure 9: Particle size distribution (A: cumulative, B: derivative) during C_3S -hydration. Measurement (NF-PXCT,
 550 HXCT) and simulation.

551 The results from the simulation and nano-tomography are displayed in Figure 9. The
 552 simulation results are obtained using the particle size distribution from NF-PXCT, degrees of
 553 hydration from section 3.1 and the shrinking core model from section 4.1. A close agreement
 554 between the particle size distributions from simulation and nano-tomography is indicated by
 555 the cumulative curves (Figure 9A) and impressively confirmed by the differential curves
 556 (Figure 9B). The error bars in that Figure refer to the standard deviation (1σ) of the NF-PXCT
 557 results that was obtained by splitting the analysed volume in three sub-volumes followed by
 558 extraction of the particles size distribution for each sub-volume. Thus, the standard deviation
 559 is a conservative approximation for the uncertainties introduced by particle statistics.

560 It is evident from Figure 9B that the simulation and the experimental results agree closely and
 561 always within the standard deviation. The quality of the results is underpinned by the fact that
 562 the curves referring to the individual hydration times are distinct from each other and fall
 563 outside the standard deviation from the other hydration times. Only in the late stage of
 564 hydration when the reaction slows down, the particles size distributions are located within the
 565 standard deviation of the curve from another hydration time (16 h and 20 h samples), see
 566 Figure 9B.

567 It is important to point out that the simulation data obtained from the shrinking core model
 568 closely agrees with the experimental data thus confirming the validity of that model - at least
 569 for the samples analysed in this study.

570 4.3.2 Quantitative evaluation of the simulation

571 The qualitative evaluation of the 'reaction zone hypothesis' shown in section 4.3.1 is now
 572 followed by quantitative tests by analysing the surface area of C_3S during hydration (Table 1).
 573 A comparison of measurements and predictions show that the surface area of C_3S decreases

574 during hydration. A close agreement between both nano-tomography techniques and the
 575 simulation is observed. The maximum deviation between different techniques was as small as
 576 0.06 m²/g (NF-PXCT versus HXCT for the anhydrous C₃S). This difference is due to difficulties
 577 in the segmentation of the HXCT-data of this sample already noted in section 3.3. The absolute
 578 differences between the methods are even smaller for all other samples with HXCT tending to
 579 give slightly lower values. The good agreement between simulation and experimental data
 580 implies that the 'reaction zone hypothesis' can predict the specific surface area of tricalcium
 581 silicate during hydration with high accuracy. This statement applies to the samples prepared
 582 in this study and a general validation of the model would require a systematic analysis of
 583 many other samples.

584 The surface area data in Table 1 refers to the outer surface of the particles and may be modified
 585 by changes in micro-roughness of the particles during hydration. It has to be kept in mind that
 586 the values reported in Table 1 account for particles larger than 124 nm as smaller particles
 587 cannot be detected by the experimental methods used in this study. The presence of smaller
 588 particles will lead to higher surface areas and can be included in the simulation. Such particles
 589 smaller than 124 nm had to be removed from the present simulation to be consistent with the
 590 experimental study. A repetition of the simulation using the particle size distribution from the
 591 laser diffraction data would derive surface area data that is systematically higher than the
 592 results in Table 1. This difference is due to the fact that laser diffraction can analyse much
 593 smaller samples as it operates on a different physical basis. Such data was not included in the
 594 current study as it cannot be compared to the experimental results obtained by nano-
 595 tomography.

596

Hydration time	Degree of hydration	Aqueous phase composition		Surface area C ₃ S with respect to 1 g alite [m ²]		
		Ca [mmol/L]	Si [μmol/L]	Ptycho-graphy	Holo-graphy	Simu-lation
[h]	[-]					
0	0.03	-	-	0.72	0.66	-
4	0.04	19.8	32.1	-	-	0.66
8	0.11	15.6	33.6	-	-	0.62
12	0.38	17.2	32.6	0.43	0.40	0.43
16	0.69	15.5	28.2	0.24	0.21	0.22
20	0.77	-	-	0.17	0.15	0.17
24	0.81	-	-	-	-	0.14

597 Table 1: Comparison of the measured and simulated evolution of the surface area of C₃S per 1 g anhydrous material
 598 during hydration. The aqueous phase composition is additionally shown.

599 In view of the quantitative comparison in Table 1, the reaction zone hypothesis enables to
 600 simulate the measured (HXCT and NF-PXCT) development of the C₃S particle sizes during
 601 hydration (at least for the samples analysed in this study). Therefore, to predict the surface
 602 area of C₃S during hydration, the starting particle size distribution and the degree of hydration
 603 of the bulk sample are sufficient as input parameters for equations (3) – (6). These reported
 604 values can be used, for example, as parameters for the simulation of the C₃S hydration kinetics
 605 during the first 24 h of hydration. For this purpose, Table 1 summarizes additionally the values
 606 obtained in the current study regarding the aqueous phase composition and related simulated

607 surface area of C_3S for the samples hydrated for 4 h, 8 h, 12 h and 16 h with respect to 1 g alite
608 at 0 h. An integration of our results into kinetic models and the discussion of basic mechanisms
609 for C_3S hydration in the light of our data is beyond the scope of this paper.

610 The reaction zone hypothesis was applied here for the computation of C_3S layer dissolved
611 during hydration and showed good agreement with the experimental data for the evolution
612 of the C_3S particle size distribution during hydration. In addition to this, the reaction zone
613 hypothesis can be applied to the thickness of the C-S-H layer formed around the C_3S particles
614 during hydration as originally proposed [8, 56, 57]. However, the evaluation of such a model
615 would require the extraction of the C-S-H rim thickness from the nano-tomography data
616 which has not been successfully realized. It was also attempted to obtain information on the
617 thickness of the hydrated rim from the SEM data but the uncertainty in the C-S-H shell
618 thickness results obtained by this method was too high. This has prevented an evaluation of
619 the reaction zone hypothesis to the C-S-H layer and such an extension can be the scope of
620 future studies.

621 5. Conclusions

622 The present study focuses on the measurement of the time-dependent C_3S particle size
623 distribution during the main hydration period of C_3S . Since the C_3S particles are overgrown
624 by C-S-H, phase selective synchrotron radiation nano-tomography was applied for the first
625 time to cementitious materials by combining two different operation modes (HXCT and NF-
626 PXCT). The obtained volume distribution of C_3S particles shows good accordance between
627 HXCT and NF-PXCT results. The experimental data indicate that the C_3S particles sizes
628 decrease during hydration, which leads to a decrease of the specific surface area of C_3S due to
629 the consumption of small particles.

630 The obtained experimental results are used to simulate the process of C_3S dissolution during
631 hydration using a constant reacted rim thickness for all C_3S particle sizes that varies with the
632 degree of hydration ('reaction zone hypothesis' [8]). For this purpose, the degree of hydration
633 of the bulk samples and the C_3S particle size distribution of the starting material are used as
634 input parameters for these simulations. The degree of hydration during the first 20 hours of
635 hydration was independently determined by means of QXRD, ^{29}Si MAS NMR, and TA with
636 consistent results. The simulation of the C_3S particle size distribution based on the "reaction
637 zone hypothesis" showed good agreement with the measured values by HXCT and NF-PXCT
638 for our samples. It has to be noted that only particles bigger than 124 nm in diameter are
639 investigated and compared to calculated values. Thus, the 'reaction zone hypothesis' appears
640 to be an adequate description of the development of the particle size distribution of C_3S during
641 hydration.

642

643 Acknowledgements

644 This work was supported by the European Synchrotron Research Facility under the project
645 number CH 5449 "Surface area of hydrated cement calculated from SR nano-tomography" to
646 F. Bellmann.

647 References

- 648 1. Taylor, H.F.W., *Cement Chemistry*. 2nd ed. 1997: Thomas Telford, London.
- 649 2. Ouzia, A. and K. Scrivener, *The needle model: A new model for the main hydration peak of*
- 650 *alite*. *Cement and Concrete Research*, 2019. **115**: p. 339-360.
- 651 3. Rößler, C., F. Steiniger, and H.-M. Ludwig, *Characterization of C-S-H and C-A-S-H*
- 652 *phases by electron microscopy imaging, diffraction, and energy dispersive X-ray spectroscopy*.
- 653 *Journal of the American Ceramic Society*, 2017. **100**(4): p. 1733-1742.
- 654 4. Möser, B. and J. Stark, *A New Model Of Ordinary Portland Cement Hydration Derived By*
- 655 *Means Of ESEM-FEG*. *Materials Science of Concrete: Cement and Concrete - Trends*
- 656 *and Challenges*, ed. A.J. Boyd, S. Mindess, and J.P. Skalny. 2002: Wiley.
- 657 5. Gartner, E.M., et al., eds. *Hydration of Portland Cement*. *Structure and Performance of*
- 658 *Cements*, ed. J. Bensted and P. Barnes. 2002. 57-113.
- 659 6. Garrault, S., et al., *Study of C-S-H growth on C3S surface during its early hydration*.
- 660 *Materials and Structures*, 2005. **38**(4): p. 435-442.
- 661 7. Kjellsen, K.O. and H. Justnes, *Revisiting the microstructure of hydrated tricalcium silicate-*
- 662 *a comparison to Portland cement*. *Cement and Concrete Composites*, 2004. **26**(8): p. 947-
- 663 956.
- 664 8. Masoero, E., J.J. Thomas, and H.M. Jennings, *A Reaction Zone Hypothesis for the Effects of*
- 665 *Particle Size and Water-to-Cement Ratio on the Early Hydration Kinetics of C3S*. *Journal of*
- 666 *the American Ceramic Society*, 2014. **97**(3): p. 967-975.
- 667 9. Bergold, S.T., F. Goetz-Neunhoeffler, and J. Neubauer, *Mechanically activated alite: New*
- 668 *insights into alite hydration*. *Cement and Concrete Research*, 2015. **76**: p. 202-211.
- 669 10. Song, Y., et al., *Pore network of cement hydrates in a High Performance Concrete by 3D*
- 670 *FIB/SEM – Implications for macroscopic fluid transport*. *Cement and Concrete Research*,
- 671 2018.
- 672 11. da Silva, Í.B., *X-ray Computed Microtomography technique applied for cementitious materials:*
- 673 *A review*. *Micron*, 2018. **107**: p. 1-8.
- 674 12. Aranda, M.A.G., *Recent studies of cements and concretes by synchrotron radiation*
- 675 *crystallographic and congrate methods*. *Crystallography Reviews*, 2015. **22**(3): p. 150-196.
- 676 13. Stampanoni, M., et al., *Coherent X-ray Imaging: Bridging the Gap between Atomic and*
- 677 *Micro-scale Investigations*. *CHIMIA International Journal for Chemistry*, 2014. **68**(1): p.
- 678 66-72.
- 679 14. Parisatto, M., et al., *Examining microstructural evolution of Portland cements by in-situ*
- 680 *synchrotron micro-tomography*. *Journal of Materials Science*, 2015. **50**(4): p. 1805-1817.
- 681 15. Cuberos, A.J.M., et al., *Phase development in conventional and active belite cement pastes by*
- 682 *Rietveld analysis and chemical constraints*. *Cement and Concrete Research*, 2009. **39**(10):
- 683 p. 833-842.
- 684 16. Álvarez-Pinazo, G., et al., *In-situ early-age hydration study of sulfoelite cements by*
- 685 *synchrotron powder diffraction*. *Cement and Concrete Research*, 2014. **56**(0): p. 12-19.
- 686 17. Artioli, G., *Powder Diffraction and Synchrotron Radiation*, in *Synchrotron Radiation: Basics,*
- 687 *Methods and Applications*, S. Mobilio, F. Boscherini, and C. Meneghini, Editors. 2014,
- 688 Springer Berlin Heidelberg.
- 689 18. De La Torre, Á.G., et al., *The superstructure of C3S from synchrotron and neutron powder*
- 690 *diffraction and its role in quantitative phase analyses*. *Cement and Concrete Research*, 2002.
- 691 **32**(9): p. 1347-1356.
- 692 19. Garbev, K., et al., *Cell Dimensions and Composition of Nanocrystalline Calcium Silicate*
- 693 *Hydrate Solid Solutions. Part 1: Synchrotron-Based X-Ray Diffraction*. *Journal of the*
- 694 *American Ceramic Society*, 2008. **91**(9): p. 3005-3014.
- 695 20. Merlini, M., et al., *The early hydration and the set of Portland cements: In situ X-ray powder*
- 696 *diffraction studies*. *Powder Diffraction*, 2012. **22**(3): p. 201-208.
- 697 21. Schlegel, M.-C., et al., *First Seconds in a Building's Life – In Situ Synchrotron X-Ray*
- 698 *Diffraction Study of Cement Hydration on the Millisecond Timescale*. *Angewandte Chemie*
- 699 *International Edition*, 2012. **51**(20): p. 4993-4996.

- 700 22. Gutberlet, T., et al., *New insights into water bonding during early tricalcium silicate*
701 *hydration with quasielastic neutron scattering*. Cement and Concrete Research, 2013. **51**(0):
702 p. 104-108.
- 703 23. Chae, S.R., et al., *Advanced Nanoscale Characterization of Cement Based Materials Using X-*
704 *Ray Synchrotron Radiation: A Review*. International Journal of Concrete Structures and
705 Materials, 2013. **7**(2): p. 95-110.
- 706 24. Monteiro, P.J.M., et al., *Characterizing the nano and micro structure of concrete to improve*
707 *its durability*. Cement and Concrete Composites, 2009. **31**(8): p. 577-584.
- 708 25. Provis, J.L., et al., *Nanostructural characterization of geopolymers by advanced beamline*
709 *techniques*. Cement and Concrete Composites, 2013. **36**: p. 56-64.
- 710 26. Brisard, S., M. Serdar, and P.J.M. Monteiro, *Multiscale X-ray tomography of cementitious*
711 *materials: A review*. Cement and Concrete Research, 2020. **128**: p. 105824.
- 712 27. Artioli, G., et al., *Direct Imaging of Nucleation Mechanisms by Synchrotron Diffraction*
713 *Micro-Tomography: Superplasticizer-Induced Change of C-S-H Nucleation in Cement*.
714 Crystal Growth & Design, 2015. **15**(1): p. 20-23.
- 715 28. Stockmar, M., et al., *Near-field ptychography: phase retrieval for inline holography using a*
716 *structured illumination*. Scientific Reports, 2013. **3**: p. 1927.
- 717 29. Monteiro, P.J.M., et al., *Advances in characterizing and understanding the microstructure of*
718 *cementitious materials*. Cement and Concrete Research, 2019. **124**: p. 105806.
- 719 30. Trtik, P., et al., *Density mapping of hardened cement paste using ptychographic X-ray*
720 *computed tomography*. Cement and Concrete Composites, 2013. **36**: p. 71-77.
- 721 31. da Silva, J.C., et al., *Mass Density and Water Content of Saturated Never-Dried Calcium*
722 *Silicate Hydrates*. Langmuir, 2015. **31**(13): p. 3779-3783.
- 723 32. Cuesta, A., et al., *Quantitative disentanglement of nanocrystalline phases in cement pastes by*
724 *synchrotron ptychographic X-ray tomography*. International Union of Crystallography
725 Journal, 2019. **6**(3): p. 473-491.
- 726 33. Cuesta, A., et al., *Chemistry and Mass Density of Aluminum Hydroxide Gel in Eco-Cements*
727 *by Ptychographic X-ray Computed Tomography*. The Journal of Physical Chemistry C,
728 2017. **121**(5): p. 3044-3054.
- 729 34. Cuesta, A., et al. *In situ hydration imaging study of a ye'elimite paste by ptychographic x-ray*
730 *computed tomography*. in *39th International Conference on Cement Microscopy ICMA*. 2017.
- 731 35. Geng, G., et al., *Synchrotron X-ray nanotomographic and spectromicroscopic study of the*
732 *tricalcium aluminate hydration in the presence of gypsum*. Cement and Concrete Research,
733 2018. **111**: p. 130-137.
- 734 36. Garrault, S., T. Behr, and A. Nonat, *Formation of the C-S-H Layer during Early Hydration*
735 *of Tricalcium Silicate Grains with Different Sizes*. The Journal of Physical Chemistry B,
736 2006. **110**(1): p. 270-275.
- 737 37. Franke, B., *Bestimmung von Calciumoxyd und Calciumhydroxyd neben wasserfreiem und*
738 *wasserhaltigem Calciumsilikat*. Zeitschrift für anorganische und allgemeine Chemie,
739 1941. **247**(1-2): p. 180-184.
- 740 38. Sowoidnich, T., et al., *Calcium complexation and cluster formation as principal modes of*
741 *action of polymers used as superplasticizer in cement systems*. Cement and Concrete
742 Research, 2015. **73**(0): p. 42-50.
- 743 39. Jiang, S.P., J.C. Mutin, and A. Nonat, *Studies on mechanism and physico-chemical*
744 *parameters at the origin of the cement setting II. Physico-chemical parameters determining the*
745 *coagulation process*. Cement and Concrete Research, 1996. **26**(3): p. 491-500.
- 746 40. Jönsson, B., et al., *Controlling the Cohesion of Cement Paste*. Langmuir, 2005. **21**(20): p.
747 9211-9221.
- 748 41. Kong, X., et al., *Retardation effect of styrene-acrylate copolymer latexes on cement hydration*.
749 Cement and Concrete Research, 2015. **75**: p. 23-41.
- 750 42. O'Connor, B.H. and M.D. Raven, *Application of the Rietveld Refinement Procedure in*
751 *Assaying Powdered Mixtures*. Powder Diffraction, 2013. **3**(1): p. 2-6.

- 752 43. Jansen, D., et al., *A remastered external standard method applied to the quantification of early*
753 *OPC hydration*. *Cement and Concrete Research*, 2011. **41**(6): p. 602-608.
- 754 44. Golovastikov, N.I., *Crystal Structure of Tricalcium Silicate, 3CaOSiO₂ = C₃S*. *Sov. Phys.*
755 *Crystallogr.*, 1975. **20**: p. 441-445.
- 756 45. Busing, W.R. and H.A. Levy, *Neutron Diffraction Study of Calcium Hydroxide*. *The Journal*
757 *of Chemical Physics*, 1957. **26**(3): p. 563-568.
- 758 46. Bergold, S.T., F. Goetz-Neunhoeffler, and J. Neubauer, *Quantitative analysis of C-S-H in*
759 *hydrating alite pastes by in-situ XRD*. *Cement and Concrete Research*, 2013. **53**: p. 119-
760 126.
- 761 47. Bellmann, F., et al., *Improved evidence for the existence of an intermediate phase during*
762 *hydration of tricalcium silicate*. *Cement and Concrete Research*, 2010. **40**(6): p. 875-884.
- 763 48. Sowoidnich, T., et al., *New insights into tricalcium silicate hydration in paste*. *Journal of the*
764 *American Ceramic Society*, 2019. **102**(5): p. 2965-2976.
- 765 49. Massiot, D., et al., *Modelling one- and two-dimensional solid-state NMR spectra*. *Magnetic*
766 *Resonance in Chemistry*, 2002. **40**(1): p. 70-76.
- 767 50. Cesar da Silva, J., et al., *Efficient concentration of high-energy x-rays for diffraction-limited*
768 *imaging resolution*. *Optica*, 2017. **4**(5): p. 492-495.
- 769 51. Barret, P. and D. Bertrandie, *Fundamental hydration kinetic features of the major cement*
770 *constituents: Ca[3]SiO[5] and beta Ca[2]SiO[4]*. *Journal de chimie physique*, 1986. **83**(11-
771 12): p. 765-775.
- 772 52. Haas, J. and A. Nonat, *From C-S-H to C-A-S-H: Experimental study and thermodynamic*
773 *modelling*. *Cement and Concrete Research*, 2015. **68**(0): p. 124-138.
- 774
775
- 776 53. Stark, J. and B. Wicht, *Zement und Kalk: Der Baustoff Als Werkstoff*, 2000: Birkhauser
777 Verlag GmbH.
- 778 54. Exner, H.E.: *Stereology and 3D Microscopy: Useful Alternatives or Competitors in the*
779 *Quantitative Analysis of Microstructures?* 2004. **23**(2): p. 73-82.
- 780 55. Neerad Phansalkar, Sumit More, Ashish Sabale and Madhuri Joshi, "Adaptive local
781 thresholding for detection of nuclei in diversity stained cytology images," *2011*
782 *International Conference on Communications and Signal Processing*, Kerala, India, 2011, pp.
783 218-220.
- 784 56. J.J. Biernacki, T. Xie, *Advanced single particle model for C₃S and alite hydration*, *J. Am.*
785 *Ceram. Soc.* 94 (7) (2011) 2037-2047.
- 786 57. T. Honorio, B. Bary, F. Benboudjema, S. Poyet, *Modeling hydration kinetics based on*
787 *boundary nucleation and space-filling growth in a fixed confined zone*, *Cem. Concr.*
788 *Res.* 83 (2016) 31-44.
- 789 58. C. Naber, F. Bellmann, J. Neubauer, *Influence of w/s ratio on alite dissolution and C-*
790 *S-H precipitation rates during hydration*, *Cem Concr Res* 134 (2020) 106087.
- 791 59. A. Zingg, L. Holzer, A. Kaech, F. Winnefeld, J. Pakusch, S. Becker, L. Gauckler, *The*
792 *microstructure of dispersed and non-dispersed fresh cement pastes -- New insight by*
793 *cryo-microscopy*, *Cem. Concr. Res.*, 38 (2008) 522-529.
- 794 60. L. Holzer, P. Gasser, A. Kaech, M. Wegmann, A. Zingg, R. Wepf, B. Muench, *Cryo-FIB-*
795 *nanotomography for quantitative analysis of particle structures in cement suspensions*,
796 *Journal of Microscopy*, 227 (2007) 216-228.
- 797 61. F. Kleiner, C. Rößler, F. Vogt, A. Osburg, & H.M. Ludwig, (2021). *Reconstruction of*
798 *calcium silicate hydrates using multiple 2D and 3D imaging techniques: Light*
799 *Microscopy, μ -CT, SEM, FIB-nT combined with EDX*. *Journal of Microscopy*.

800
801
802
803
804